Journal of the European Ceramic Society 40 (2020) 742–750

Contents lists available at ScienceDirect

Journal of the European Ceramic Society

journal homepage: www.elsevier.com/locate/jeurceramsoc

Original Article

Thermoelectric properties of the textured $Bi_{1.9}Gd_{0.1}Te_3$ compounds spark-plasma-sintered at various temperatures

Maxim Yaprintsev[a], Alexei Vasil'ev[a], Oleg Ivanov[a,b,*]

[a] Belgorod State University, Belgorod 308015, Russian Federation
[b] Belgorod State Technological University Named After V.G. Shukhov, Belgorod 308012, Russian Federation

ARTICLE INFO

Keywords:
Bismuth telluride
Spark plasma sintering
Thermoelectric properties
Anisotropy
Textured grain structure

ABSTRACT

Elemental composition, crystal and grain structures, specific electrical resistivity, Seebeck coefficient, thermal conductivity, and thermoelectric figure-of-merit of n-type grained $Bi_{1.9}Gd_{0.1}Te_3$ compounds, spark-plasma-sintered at T_S = 690, 720, 750, 780 and 810 K, have been studied. All the samples are highly textured along the 001 direction parallel to the pressing direction. The average grain size measured along the pressing direction is much less as compared to the average grain size measured in the perpendicular direction. A strong anisotropy in the transport properties measured along directions parallel and perpendicular to the pressing direction was found within the 290 ÷ 630 K interval. Electrical resistivity decreases and thermal conductivity increases for parallel orientation as compared to these properties for perpendicular orientation. The T_S - effect on thermoelectric figure-of-merit of textured $Bi_{1.9}Gd_{0.1}Te_3$ compounds has been found and analyzed. Highest thermoelectric figure-of-merit (~0.75) was observed for sample with T_S = 750 K at perpendicular orientation.

1. Introduction

Today, thermoelectric materials directly conversing thermal energy into electricity and no harmful effect on the environment can fairly be considered as ones of prospect materials to develop so-called "green" energy. The thermoelectric performance of a thermoelectric material can be expressed by the dimensionless thermoelectric figure-of-merit, $ZT = TS^2/\rho k_t$, where T is the absolute temperature, S is the Seebeck coefficient, ρ is the specific electrical resistivity and k_t is the total thermal conductivity with contributions from crystal lattice, carriers and bipolar conductivity [1]. The ZT value for the conventional thermoelectrics is close to unity up to now. Unfortunately, this value is very low for industrial large-scale developing the thermoelectric generation. Analyzing the ZT definition, one can conclude that enhancing in direct heat-energy conversion is related to optimizing all three thermoelectric properties (S, ρ and k), simultaneously governing ZT. Already for a long time, bismuth telluride, Bi_2Te_3, and its n- and p- types alloys have been used as the best materials for low-temperature thermoelectric applications [2,3]. However, at present the thermoelectric efficiency of these materials still remains low enough (usually $ZT \leq 1.4$). To enhance the thermoelectric conversion efficiency, many efforts based on various modern scientific and technological approaches (like fabrication of various nanostructures, specific doping to form resonant levels and etc.), focusing on optimal S, ρ and k combination of the Bi_2Te_3-based compounds, have been made in past decades [4–15]. In turn, to extract the highest efficiency of the advantages, characteristic for these approaches, and, hence, maximize ZT, some relevant material characteristics including the density, the crystal and grain structures, the texturing degree, the phase and elemental compositions, and the specific defect structure should thoroughly be tuned during a fabrication process of the thermoelectric. One of effective and promising ways to improve the thermoelectric properties of the Bi_2Te_3-based compounds is an element doping [16–18]. Recently it was found that rare earth elements, R, (R = Lu, Ce, Sm, Er, La, Gd, etc.) can successfully be used as dopants to remarkably enhance the thermoelectric performance of Bi_2Te_3 [19–29]. The $Bi_{1.9}R_{0.1}Te_3$ composition is known to be optimal one to get a maximum ZT enhancement for R-doped Bi_2Te_3 compounds [19,29]. In this case, the R-doping effect will also be dependent on the material characteristics listed above. The material characteristics can be tuned by varying in some technological variables. Sintering temperature is one of such easily changeable and controlled variables.

The purpose of this paper is to find and analyze the patterns of sintering temperature effect on the thermoelectric properties of the n-type grained $Bi_{1.9}Gd_{0.1}Te_3$ compounds prepared by spark plasma sintering (SPS). It should also be noted that the SPS method allows preparing textured samples [30–34]. The texturing is important material characteristic effecting on the thermoelectric properties of the grained Bi_2Te_3-based compounds.

* Corresponding author at: Belgorod State University, Belgorod 308015, Russian Federation.
E-mail address: Ivanov.Oleg@bsu.edu.ru (O. Ivanov).

https://doi.org/10.1016/j.jeurceramsoc.2019.11.028
Received 2 September 2019; Received in revised form 6 November 2019; Accepted 8 November 2019
Available online 09 November 2019

2. Materials and methods

Microwave-solvothermal synthesis was used to prepare a starting $Bi_{1.9}Gd_{0.1}Te_3$ powder. Synthesis conditions and characterization results of the starting powder were reported in detail in Ref. [35]. In brief, analytically pure chemicals ($Bi(NO_3)_3{\cdot}5H_2O$, TeO_2, $Gd(CH_3COO)_3{\cdot}4H_2O$, NaOH, poly(1-ethenylpyrrolidin-2-one), ethane-1,2-diol) were used to synthesize a starting powder. At first, $Bi(NO_3)_3{\cdot}5H_2O$, TeO_2 and $Gd(CH_3COO)_3{\cdot}4H_2O$ were dissolving in mixture of 450 cm^3 ethane-1,2-diol NaOH and 15 g NaOH under vigorous stirring by a magnetic stirrer. Then, poly(1-ethenylpyrrolidin-2-one) (M_r = 12 000) was added to the reaction mixture. This mixture was again under vigorous stirring for 30 min. Finally, the autoclave was sealed and maintained at 190 °C for 18 h. After, the autoclave was naturally cooled to room temperature. As soon as the reaction was completed, dark gray precipitate was taken out by centrifuging and washed with deionized water and ethyl alcohol several times and then dried at 80 °C for 8 h. The synthesized powder was single hexagonal $R\bar{3}m$ phase, characteristic for pure Bi_2Te_3, and mainly consisted of hexagonal plates with average plate size of a few hundreds of nm and width of ~100 nm. Content of Bi, Gd and Te was equal to 38.00, 2.00 and 60.00 at. %, respectively, that is correctly corresponding to the $Bi_{1.9}Gd_{0.1}Te_3$ composition. Besides, all the elements were found to be uniformly distributed within the hexagonal $Bi_{1.9}Gd_{0.1}Te_3$ plates.

Spark plasma sintering method by using a SPS-25/10 system was applied to compact the powder at pressure of 40 MPa and sintering time of 5 min, resulting in the Ø20 mm × 15 mm cylinders. Different SPS temperatures, T_S, equal to 690, 720, 735, 750, 780, and 810 K were used. To study the thermoelectric properties, the 2 × 2 × 10 mm bars and the Ø10 × 2 mm disks were cut out both along in-plane and out of plane directions of the cylinders.

Density of the bulk samples SPS-prepared at different temperatures was measured by the Archimedes method. To identify crystal structure and phase composition of the starting powder and the bulk materials, X-ray diffraction (XRD) analysis was performed by using a Rigaku Ultima IV diffractometer with CuK_α – radiation. To determine correct elemental composition of the bulk samples, a Shimadzu ICP (Inductively Coupled Plasma) emission spectrometer ICPE-9000 was applied. A scanning electron microscope (SEM) Nova NanoSEM 450 was applied to study grain structure features of the bulk samples. The specific electrical resistivity and the Seebeck coefficient of the bar samples were measured by using a ZEM-3 system. To determine the total thermal conductivity of the disk-shaped samples, a TC-1200 system using a laser flash method was applied. A Mini Cryogen Free Measurements System (Cryogenic Ltd, UK) was also used to study the Hall effect and estimate the concentration, n, and Hall mobility, μ_H, of majority charge carriers.

3. Results and discussion

3.1. SPS-temperature effect on elemental composition, crystal and grain structure, and texturing

According to XRD patterns taken for room temperature, the bulk $Bi_{1.9}Gd_{0.1}Te_3$ samples sintered at different T_S have the crystal structure corresponding to the space symmetry $R\bar{3}m$ group like the starting powder. Therefore, the crystal symmetry does not change with varying T_S. But, the lattice c and a = b parameters were found to be weakly increased with increasing T_S (Fig. S1(a)). This behavior can be originated from changing in elemental composition due to high-temperature Te evaporation during SPS-process [21]. As a result, the Te content is gradually decreasing with increasing T_S (Fig. S1(b)). Decreasing in the Te content leads to forming Te vacancies [36]. In turn, these vacancies can generate anti-site defects of Bi in Te-sites (Bi_{Te}) [37,38]. Since ionic radius of Bi^{3+} is bigger as compared to that for Te^{2+} (1.02 nm against 0.089 nm [39]), forming the Bi_{Te} defects will really be accompanied by increasing in the lattice parameters. Thus, forming these defects can be taken as dominant mechanism, responsible for growth of the lattice parameters with decreasing the Te content.

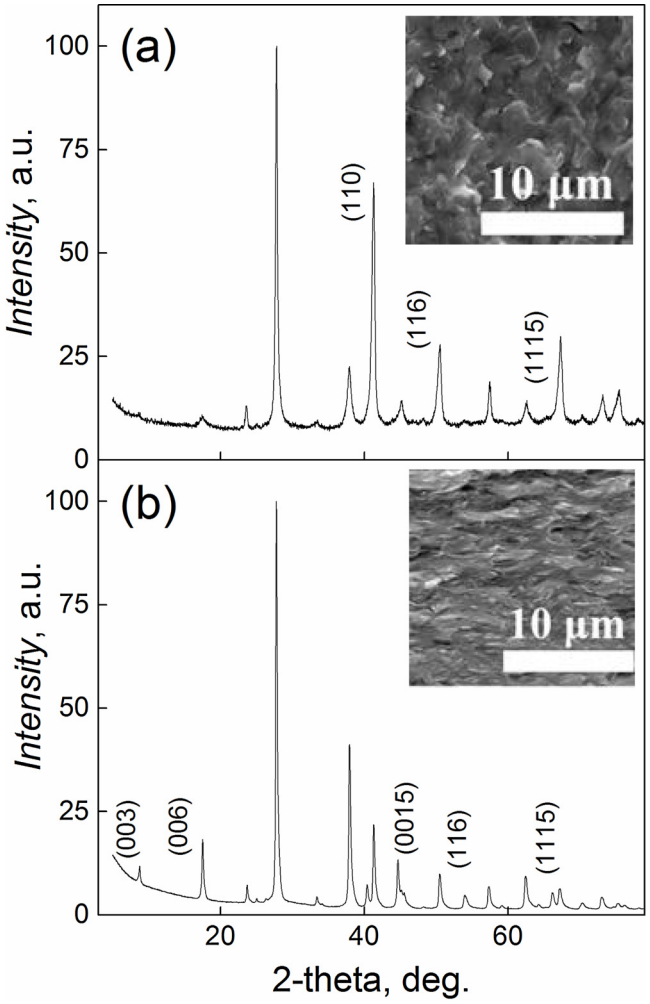

Fig. 1. (a) The XRD pattern for the bulk sample sintered at T_S = 750 K and taken on surface perpendicular to the SPS-pressing direction; (b) The XRD pattern for the same bulk sample taken on surface parallel to the SPS-pressing direction. Insets to Figs. (a) and (b) show the SEM-images taken on the fractured surfaces oriented perpendicular and parallel to the SPS- pressing direction, respectively.

Density of all the samples SPS-prepared at various temperatures was found to be nonmonotonously changed from ~6.4 g cm^{-3} (T_S = 810 K) to ~7.5 g cm^{-3} (T_S = 750 K), that are 83 % and 97 % of theoretical value of the Bi_2Te_3 density (7.7 g/cm^3).

Two features in the grain structure of the bulk $Bi_{1.9}Gd_{0.1}Te_3$ samples were found. First of them is texturing developing under SPS-process. The second feature is related to significant growth of the grains with increasing T_S. Texturing development is clearly confirmed by XRD and SEM experiments. Since the grains in the textured samples are preferentially arranged in plane oriented perpendicularly to the SPS-pressing direction, the XRD patterns, collected on surfaces perpendicular and parallel to this direction, should be rather different. These XRD patterns, recordered for the sample with T_S = 750 K, are presented in Fig. 1(a) (perpendicularly to the SPS-pressing direction) and Fig. 1(b) (parallel to the SPS-pressing direction). All the peaks at these XRD patterns can again be assigned to rhombohedral $R\bar{3}m$ structure, but the intensities of some peaks are remarkably different. The intensities of the (11l) peaks taken for surface oriented perpendicularly are found to be enhanced (Fig. 1(a)), whereas at the XRD pattern taken for parallel surface orientation, similar enhancing in the intensities is already

observed for the (001) peaks (Fig. 1(b)). Such redistribution in the intensities of the peaks can be originated from forming a lamellar texture, characterizing with preferential grain orientating during SPS-process. To show this redistribution in detail, the XRD pattern for the starting $Bi_{1.9}Gd_{0.1}Te_3$ is presented in Fig. S2. In the textured samples, the c-axes of the grains are preferentially directed parallel to the SPS-pressing direction, while the a–b planes of the grains are preferentially oriented perpendicularly to this direction. A degree of the preferential grains orientation is estimated by an orientation factor, F, which can be expressed as [30,31]

$$F = \frac{p - p_0}{1 - p_0}, \quad (1)$$

where p and p_0 are in turn expressed as

$$p = \frac{I(00l)}{\sum I(hkl)}, \quad \text{and} \quad p_0 = \frac{I_0(00l)}{\sum I_0(hkl)} \quad (2)$$

Here, the I and I_0 intensities are corresponding to oriented (textured) and non-oriented (non-textured) samples, respectively. Ideally, F = 1 is corresponding to completely oriented sample (single crystal), whereas F = 0 is characteristic of completely non-oriented sample (powder or grained material with completely random grain orientation).

The XRD patterns taken on surfaces perpendicular and parallel to the SPS-pressing direction were used to calculate the p and p_0 values, and estimate F for all the samples with different T_S. At first, F is increasing with increasing T_S from 0.59 (at T_S = 690 K) up to 0.68 (at T_S = 750 K), but at further increasing in T_S, the orientation factor is already decreasing down to 0.58 (at T_S = 810 K). The texturing is also observed in the SEM-images of the grain structures. These images recorded on the fractured surfaces oriented perpendicularly and parallel to the SPS-pressing direction for the sample with T_S = 750 are presented in inset to Fig. 1(a) and (b), respectively. Disordered grain structure with a few μm grains having mainly irregular shape is observed at the perependicular surface, whereas at parallel surface the grains form ordered lamellar structure. The lamellar sheets lie in plane perpendicular to the SPS-pressing direction. The lamellar sheets consist of the grains elongated in plane perpendicular to the SPS-pressing direction. The grain sizes in the directions perpendicular ($D_\parallel$) parallel and ($D_\perp$) to the SPS-pressing direction happen to be rather different. Besides, the grains themselves are significantly growing with increasing T_S. To estimate the average grain size in both directions, the histograms of the grain size distribution for the samples sintered at different T_S were plotted and analyzed in frames of the lognormal unimodal distribution [40]. The $D_\perp(T_S)$ and $D_\parallel(T_S)$ dependences are shown in Fig. S3. The $D_\perp$ values are much bigger as compared to the $D_\parallel$ values. Besides, both average sizes are steady increasing with increasing T_S. The grain growth during a powder material sintering is known to be usually governing by reducing in energy of system having numerous interfaces [41]. To characterize the difference in the grain sizes measured along to the both directions mentioned, a $D_\parallel/D_\perp$ ratio can be introduced as a grain shape factor. This factor can be considered as the main material parameter governing the texturing and, hence, the density of the textured material (Fig. S4).

It should be noted that the physical properties of the Bi_2Te_3 compound is inherently anisotropic [1]. The anisotropy is originated from features in crystal structure and chemical bonding. The crystal structure is layered one, and crystal a–b planes are oriented along the layers, whereas crystal c-axe are perpendicular to the layers. The chemical bonding between atoms within the layers is dominantly strong covalent, whereas neighboring layers are bonded via weak van der Waals forces. Due to various nature of the bonding environment mentioned, the physical properties measured along or perpendicular to the layers happen to be remarkably different, too. To estimate this difference in the properties, relevant anisotropy coefficients can be introduced. For the Bi_2Te_3 single crystals, anisotropy coefficients in the specific electrical resistivity, ρ, and in the thermal conductivity, k, are usually equal to $\rho_c/\rho_{ab} \approx 5 \div 5.5$ and $k_{ab}/k_c \approx 2$, respectively [1,42,43]. Here the ab and c subscripts corresponds to the ρ and k measuring directions, oriented either along with the crystal a–b plane or along with the crystal c-axis, respectively. Since ρ and k for the Bi_2Te_3 single crystals are highly anisotropic, the thermoelectric figure-of-merit happens to be anisotropic, too. For the grained material with completely random orientation of the grains, ZT is already isotropic. The texturing resulting in preferential grain orientation can recover, at least, partially the anisotropy in the transport properties. In this case, some physical properties, measured along the texturing direction or within the plane perpendicular to this direction, start to be different again.

3.2. SPS-temperature effect on concentration and Hall mobility of the majority carriers

The concentration and the Hall mobility of the majority carriers were extracted by study of the Hall effect at room temperature. The Hall constant, R_H, was found to have a negative sign for all the samples, i.e. the majority carriers in these samples are electrons. The electron concentration was then estimated by using a link between R_H and n expressed as $R_H = 1/(n \cdot e)$ [44]. The Hall mobility of the electrons was estimated by using the $\mu_H = (R_H/\rho)$ ratio. Due to the partially recovered anisotropy in the physical properties of Bi_2Te_3, the specific electrical resistivity of the textured compound is usually different for the measurement direction perpendicular to the SPS-pressing direction (perpendicular orientation), and the measurement direction parallel to the SPS-pressing direction (parallel orientation). So, two values of the Hall mobility corresponding to the perpendicular ($\mu_{H\perp}$) and parallel ($\mu_{H\parallel}$) orientations should be analyzed. The $n(T_S)$, $\mu_{H\perp}(T_S)$ and $\mu_{H\parallel}(T_S)$ dependences are presented in Fig. 2.

Both the electron concentration and the Hall mobilities are increasing with increasing T_S, demonstrating a rather complicated behavior. The $\mu_{H\perp}$ mobility is much bigger than the $\mu_{H\parallel}$, whereas the electron concentration is naturally the same for both parallel and perpendicular orientations. The T_S-effect on n, $\mu_{H\perp}$ and $\mu_{H\parallel}$ can be due to a combination of several different mechanisms depending on T_S and acting simultaneously. At present, to distinguish these concrete mechanisms correctly is a complicated task. However, dominant mechanisms governing the $n(T_S)$, $\mu_{H\perp}(T_S)$ and $\mu_{H\parallel}(T_S)$ dependences can still be found. Let us consider the main mechanism resulting in the increasing in n with increasing T_S. It is known [16–18] that both type and concentration of the carriers in Bi_2Te_3 are closely related to various point defects. Since at high temperatures the Te evaporation takes place, the most common defects are vacancies at Te sites, $V_{Te}^{\bullet\bullet}$. Each positively charged $V_{Te}^{\bullet\bullet}$ vacancy will leave two free electrons. This process can be described by equation

$$Bi_2Te_3 = 2Bi_{Bi}^{\times} + 2Te_{Te}^{\times} + Te(g) + V_{Te}^{\bullet\bullet} + 2e', \quad (3)$$

where symbol g is corresponding to a gaseous phase.

Then, the electron concentration should be increasing with decreasing Te content (or with increasing in number of the Te vacancies). This tendency was really observed in our experiment (Fig. 3(a)). Besides this main mechanism, other mechanisms can also contribute to the $n(T_S)$ behavior. Two mechanisms, at least, related to (i) appearing the dangling bonds at grain boundaries due to Te deficiencies, and (ii) forming the anti-site Bi_{Te} defects at high temperatures should be considered. The dangling bonds at the grain boundaries, forming via Te deficiency, can be considered as fractional- $V_{Te}^{\bullet\bullet}$ vacancies. These vacancies behave as n-type dopants similarly to whole- $V_{Te}^{\bullet\bullet}$ defects inside the grains. In this case, the electron concentration should gradually be increasing, when the grain boundaries area per unit volume is increasing, too. In turn, the grain boundary area per unit volume should gradually be increasing, when the average grain size is, in contrast, decreased. However, in our experiment increasing in the average grain size with increasing T_S is accompanied by increasing in n. Therefore, the dangling bonds contribution is not dominant mechanism, effecting

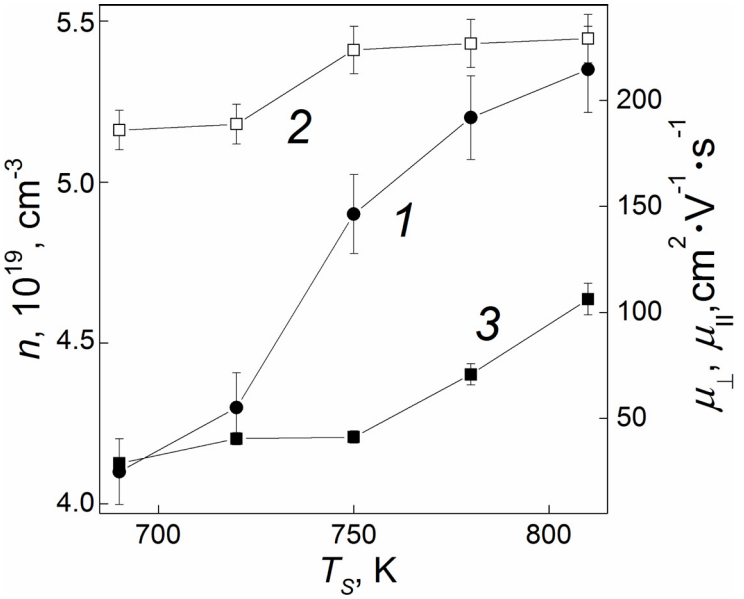

Fig. 2. The $n(T_S)$ (curve 1), $\mu_{H\perp}(T_S)$ (2) and $\mu_{H\parallel}$ (3) vs. T_S dependences.

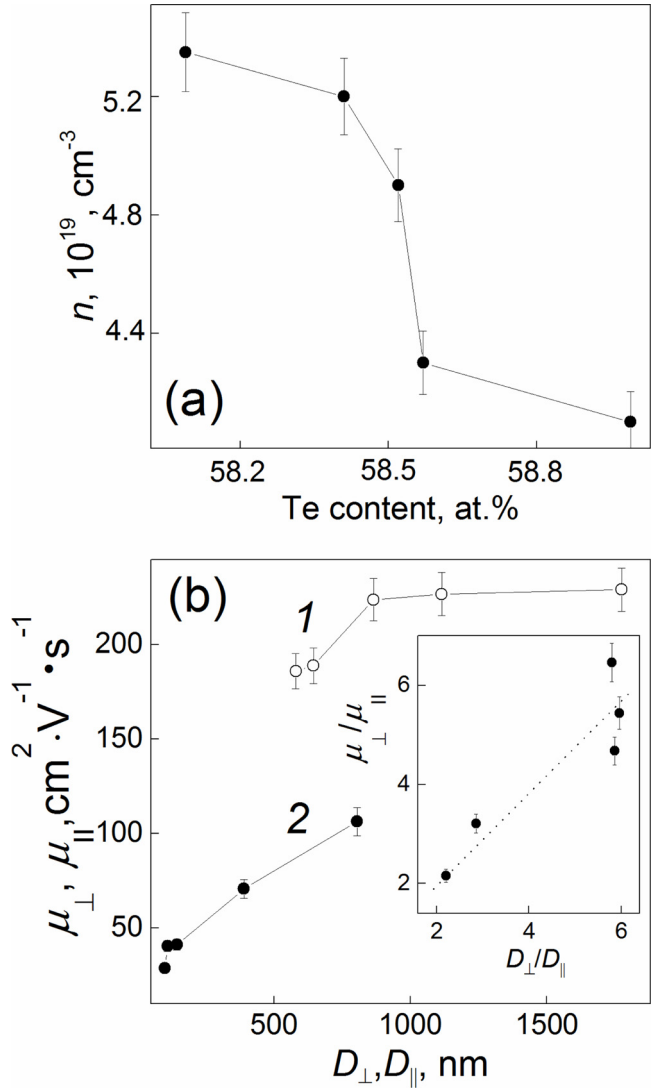

Fig. 3. (a) The n vs. Te content dependence; (b) the $\mu_{H\perp}$ vs. $D_\perp$ (curve 1) and $\mu_{H\parallel}$ vs. $D_\parallel$ (2) dependences. Inset: the $\mu_{H\perp}/\mu_{H\parallel}$ vs. $D_\perp/D_\parallel$ dependence.

on the $n(T_S)$ behavior. Forming the anti-site Bi_{Te} defects at high temperatures was before applied to account for increasing in the lattice c and a parameters with increasing T_S (Fig. S1(a)). Each forming Bi_{Te} defect will contribute one hole as a free carrier reducing a fraction of the electrons as the majority carriers. This process should also result in decreasing in n with increasing in the anti-site Bi_{Te} defects content (or with increasing T_S), that is contrary to the experiment. Thus, if the dangling bonds and anti-site Bi_{Te} defects contributions still occur, they are minor ones as compared to the dominant contribution due to the $V_{Te}^{\bullet\bullet}$ vacancies.

Difference in $\mu_{H\perp}$ and $\mu_{H\parallel}$ for the textured samples can be attributed to a few mechanisms. The mobility is usually related to various defects acting as scattering centres. For the samples studied, the typical defects sensitive to changing in T_S are the $V_{Te}^{\bullet\bullet}$ vacancies, the anti-site Bi_{Te} defects and the grain boundaries. It was found that both $\mu_{H\perp}$ and $\mu_{H\parallel}$ are strongly dependent on the relevant average grain size (Fig. 3(b)). Hence, of all these typical defects, the grain boundary scattering can reasonably be considered as the dominant mechanism effecting on the $\mu_{H\perp}(T_S)$ and $\mu_{H\parallel}(T_S)$ dependences. As a rule, the grain boundary scattering is usually effective one for micro- and nanostructural materials [45,46]. The average grain size for the textured $Bi_{1.9}Gd_{0.1}Te_3$ compounds was found to be very different for the directions perpendicular and parallel to the SPS-pressing direction. More number of the grain boundaries acting as the scattering centers exist for the parallel orientation. So, for this orientation the grain boundary scattering should be more effective.

The Mayadas-Shatzkes model can be applied to analyze the effect of the grain boundaries on the electrical resistivity [47]. In accordance with the Mayadas-Shatzkes model, the grain boundaries can be regarded as potential barriers which have to be overcome by the electrons. The scattering electron processes from the potential barriers will result in decreasing in the electron mobility. A relation between the electron mobility due to the grain boundary scattering, μ_{GB}, and the electron mobility of the grainless materials, μ_{cryst}, is expressed as [48]

$$\frac{\mu_{GB}}{\mu_{cryst}} \approx \frac{1}{1 + 1.34\left(\frac{R}{1-R}\right)\frac{l_e}{D}} \quad (4)$$

where R is the reflectivity of the grain boundaries, l_e is the electron mean free path and D is the average grain size.

The μ_{cryst} mobility determines the bulk resistivity of the grained material, whereas the μ_{GB} mobility is related to additional resistivity

contribution due to the grain boundaries. In accordance with expression (4), decreasing in D will result in decreasing in μ_{GB}. The experimental results confirm this conclusion (Fig. 3(b)). It should be noted that at $T_S \geq 750$ K, $D_\perp$ and $D_\parallel$ are rapidly growing (Fig. S3). The growth is accompanied by increasing in $\mu_{H\perp}$ and $\mu_{H\parallel}$. The $\mu_{H\perp}$ mobility is clearly saturated at $D_\perp \geq \sim 1000$ nm, i.e. the grain boundary scattering becomes ineffective for the coarse-grained samples. Changing in grain shape factor with varying T_S can also result in anisotropic behavior of the Hall mobilities. Really, the increasing in $D_\perp/D_\parallel$ is accompanied by the relevant increasing in $\mu_{H\perp}/\mu_{H\parallel}$ (inset to Fig. 3(b)).

3.3. SPS-temperature effect on the thermoelectric properties

In our experiment, all the thermoelectric properties including the specific electrical resistance, the Seebeck coefficient and the total thermal conductivity of the grained $Bi_{1.9}Gd_{0.1}Te_3$ samples happened to be T_S-dependent. Since the samples studied were highly-textured, these properties were found to be anisotropic. To take into account the texturing effect, we will analyze the T_S-effect on the thermoelectric properties for the perpendicular and parallel orientations of the measurement.

Fig. 4 shows the T_S-effect on the specific electrical resistance (a), the Seebeck coefficient (b) and the power factor (c) calculated as S^2/ρ taken at perpendicular (left panel) and parallel (right panel) orientations of measurement. All the dependences are presented in the same scale. The ρ is gradually decreasing with increasing T_S for both orientations excepting the $\rho_\perp$ behaviour for the perpendicular orientation in the samples with $T_S = 780$ and 810 K (for these samples the $\rho_\perp(T)$ curves at $T > \sim 500$ K lie above the $\rho_\perp(T)$ curve taken for the sample with $T_S = 750$ K, see inset to Fig. 4(a)). The electrical resistivity for the parallel orientation is much more as compared to the perpendicular orientation. As for the ρ(T) dependences, ρ of all the samples is gradually increasing with increasing temperature within whole temperature range from 290 up to 630 K. It is known that the specific electrical resistance of donor semiconductors can be expressed as $\rho = 1/(e\mu n)$ [49]. Then, the temperature ρ changes in Fig. 4(a) can be originated from the μ(T) and n(T) changes.

The Seebeck coefficient for all the samples has a negative sign characteristic for n-type conductivity (Fig. 4(b)). The T_S - effect on S is rather weak. Of all the S(T) curves, the Seebeck coefficient is highest for the perpendicular measurement orientation at $T_S = 750$ K. In this case, S is enhancing by ~5 %. All the S(T) curves were found to have the maxima centered at temperature of ~450 K. These maxima are originated from a bipolar effect characteristic of the doped Bi_2Te_3 and Bi_2Te_3-based compounds [27–29]. The S(T) dependences can also be used to estimate the band gap, E_g. In accordance with the Goldsmid-Sharp expression, E_g, the maximum value of the Seebeck coefficient ($|S|_{max}$) and the temperature at which it occurs (T_{max}), are related by expression $E_g = 2e\,|S|_{max}\,T_{max}$ [50]. The Goldsmid-Sharp expression results in the E_g estimate equal to ~0.14 eV for all the samples studied. This estimate is in well accordance with the band gap value known for Bi_2Te_3 [2]. The temperature dependences of the power factor are presented in Fig. 4(c). These dependences account for the ρ and S contributions. Since ρ for the perpendicular orientations is much lower than ρ for the parallel orientation, the power factor for the perpendicular orientation (left panel) is far less the power factor for the parallel orientation (right panel). Of all the power factor values calculated for the perpendicular orientation, the highest value is observed for the sample with $T_S = 750$ K. The highest S^2/ρ value for the parallel orientation is observed for the sample $T_S = 810$ K. This sample has the lowest ρ value.

The temperature dependences of the total thermal conductivity (k_t) of the samples are shown in Fig. 5(a). Due to partial recovering in natural anisotropy, $k_{t\perp}$ for the perpendicular orientations happens to be higher as compared to $k_{t\parallel}$ for the parallel orientations. Besides, all the $k_t(T)$ curves have minima positioned at ~400 K. In comparison with the $\rho(T_S)$ behavior (Fig. 4(a)), the total thermal conductivity behaves in opposite manner, i.e. both $k_{t\perp}$ and $k_{t\parallel}$ are gradually increasing with increasing T_S for both orientations excepting the $k_{t\perp}$ behaviour for the perpendicular orientation in the samples with $T_S = 780$ and 810 K (for these samples the $k_{t\perp}(T)$ curves at $T > \sim 500$ K lie below the $k_{t\perp}(T)$ curve taken for the sample with $T_S = 750$ K. Like the T_S-effect on $\rho_\perp$ and $\rho_{0\parallel}$, the T_S-effect on $k_{t\perp}$ for the parallel orientation is also expressed much more as compared to that for the perpendicular orientation.

In general, the lattice (or phonon) thermal conductivity, k_p, the electronic thermal conductivity, k_e, and the bipolar thermal conductivity, k_b, contribute to k_t. The electronic thermal conductivity is related to the specific electrical conductivity, $\sigma = 1/\rho$, through the Wiedemann-Franz law, $k_e = L\sigma T$, where L is the Lorenz number [8]. The Wiedemann-Franz law was originally developed for metals, for which the Lorenz number is equal to 2.45×10^{-8} WΩ K^{-2}. But, this L value is often incorrect to be used for the semiconductors, since the Lorenz number is dependent on the Fermi level position. Approach proposed in Ref. [51] can be applied to estimate the Lorenz number more correctly. Under this approach a relation between L and the maximum value of the Seebeck coefficient is taken into account as follows

$$L\,[10^{-8},\ W\bullet\Omega\bullet K^{-2}] = 1.5 + exp\left(-\frac{|S|_{max}\,[\mu V\bullet K^{-1}]}{116}\right) \quad (5)$$

By using expression (8), the Lorenz number was estimated as $\sim 1.8 \times 10^{-8}$ WΩ K^{-2} for all the samples studied. This L value was used to extract the $k_e(T)$ contributions to the total thermal conductivity, as is shown in Fig. 5(b). Due to lower electrical resistivity, the $k_{e\perp}$ contribution for the perpendicular orientation is much more as compared to that for the parallel orientation. Although all the ρ(T) dependences are growing with increasing T (Fig. 4(a)), the $k_e(T)$ dependences for both measurement orientations can be either falling or growing depending on the ρ values. Sums of the lattice and bipolar thermal conductivity contributions were extracted as $k_p(T) + k_b(T) = k_t(T) - k_e(T)$ (Fig. 5(c)). For the parallel orientation, the $k_p(T) + k_b(T)$ contribution is increasing with increasing T_S, but no clear correlation between the $(k_p + k_b)_\perp - T$ curves and T_S can be found for the perpendicular orientation. All the $k_p(T) + k_b(T)$ curves have minima at temperature of ~400 K. For temperatures below the minima, the summarized $k_p(T) + k_b(T)$ contributions to the total thermal conductivity are gradually decreasing with increasing temperature. This behavior can be attributed to the lattice thermal conductivity. Above the Debye temperature, the lattice thermal conductivity is usually varied as T^{-1} [52]. According to the Dulong-Petit law, the phonon specific heat is a constant for these temperatures and phonon energy increases linearly with increasing temperature, i.e. with increasing T the number of phonons increases linearly. The experimental $k_p(T)$ dependences really obey the $k_p \sim T^{-1}$ law for temperatures below minima in the $k_p(T) + k_b(T)$ curves shown by dashed lines in Fig. 5 (c). Above the minima in the $k_p(T) + k_b(T)$ curves, these summarized contributions already increase as temperature increases. This growth can be related to the bipolar thermal conductivity [53].

Finally, the ρ(T), S(T) and $k_t(T)$ contributions measured for both orientations were used to calculate the ZT(T) dependences (Fig. 6).

The thermoelectric figure-of-merit for the perpendicular orientation is much more as compared to that for the parallel orientation. For the perpendicular orientation, low ρ favoring to enhancing in ZT, but high k_t harmful for final enhancing in ZT, are simultaneously observed. However, the ρ contribution is dominant, that results in enhancing in ZT. All the curves in Fig. 6 are bell-like shaped with maxima temperatures falling in the 450 − 470 K interval and weakly depending on T_S. These maxima are originated from the intrinsic conductivity developing at high temperatures and resulting in the bipolar thermal conductivity. The bipolar thermal conductivity results in remarkable degrading in thermoelectric efficiency at high temperatures. The T_S-

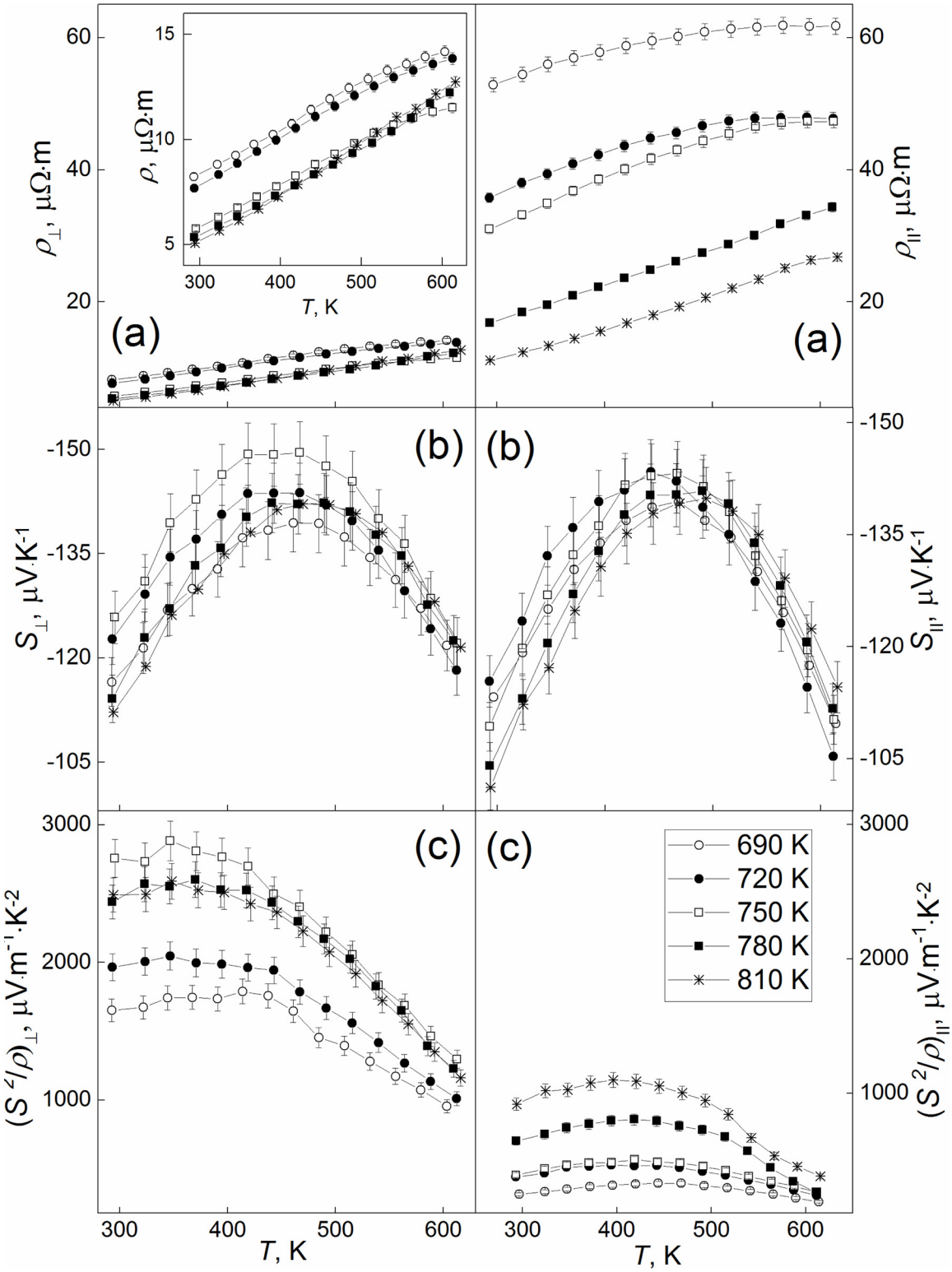

Fig. 4. The sintering temperature effect on ρ (a), S (b) and S^2/ρ (c) for the perpendicular (left panel) and parallel (right panel) orientations.

effect on the thermoelectric figure-of-merit of the textured $Bi_{1.9}Gd_{0.1}Te_3$ compounds is clearly expressed (inset to Fig. 6, right panel). The optimal ρ, k_t and S combination is observed for the sample with T_S = 750 K at the perpendicular measurement orientation. This sample is characterized by the highest orientation factor and density, too.

4. Conclusion

Thus, the thermoelectric properties of n-type grained $Bi_{1.9}Gd_{0.1}Te_3$ compounds, SPS-prepared at different temperatures, are happened to be rather sensitive to the sintering temperature. This sensitivity is mainly governed by three factors. The first of them is related to the texturing developing under the SPS-loading, and the texturing degree is T_S-dependent. The texturing is just redistributing the anisotropic

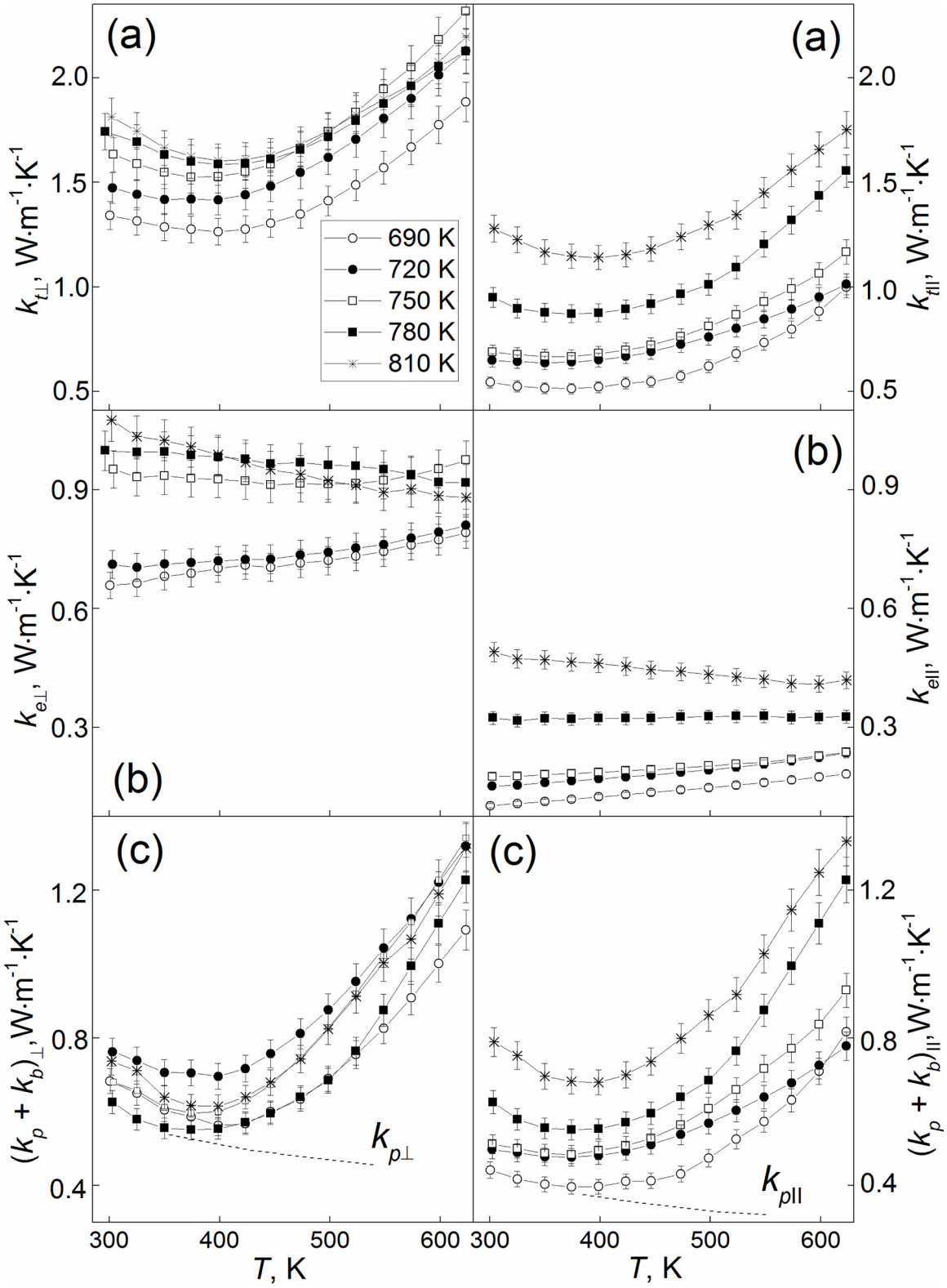

Fig. 5. The sintering temperature effect on k_t (a), (b), and (k_p + k_b) (c) for the perpendicular (left panel) and parallel (right panel) orientations.

contributions from the crystal a–b plane and c-axis to the transport properties measured for the perpendicular and parallel orientations. The redistributing degree is determined by the orientation factor depending on T_S. The second factor is the grains growth with increasing sintering temperature, and the growth rate is, firstly, T_S-dependent, and, secondly, different for the directions perpendicular and parallel to the SPS-pressing direction. Therefore, the grain shape factor is happening to be T_S-dependent, and the grain boundary scattering of the electrons and the phonons, effecting on the specific electrical resistivity and the thermal conductivity, is also depending on T_S. Finally, with increasing T_S the electron concentration is also increasing. This feature is due to forming the Te-vacancies at high temperatures that is additionally effecting on the specific electrical resistivity.

Detailed analysis of the T_S-effect on the temperature behavior in the

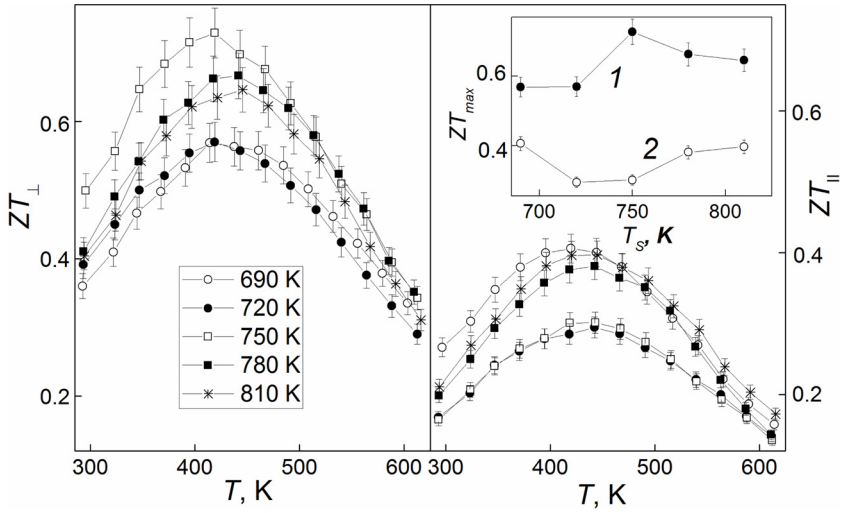

Fig. 6. The sintering temperature effect on ZT for the perpendicular (left panel) and parallel (right panel) orientations. Inset: The ZT_{max} vs. T_S dependences for the perpendicular (curve 1) and parallel (2) orientations.

thermoelectric properties of the grained $Bi_{1.9}Gd_{0.1}Te_3$ compounds will be published elsewhere.

Declaration of Competing Interest

None.

Acknowledgements

This research was funded by the Ministry of Education and Science, Russia, under Grant No. 11.3719.2017/PCh (11.3719.2017/4.6). All of studies were carried out by the scientific equipment of joint research center "Technologies and Materials" at the Belgorod State University.

Appendix A. Supplementary data

Supplementary material related to this article can be found, in the online version, at doi:https://doi.org/10.1016/j.jeurceramsoc.2019.11.028.

References

[1] G.S. Nolas, J. Sharp, H.J. Goldsmid, Thermoelectrics Basic Principles and New Materials Developments, Springer, Berlin, 2001.
[2] H.J. Goldsmid, Bismuth telluride and its alloys as materials for thermoelectric generation, Materials 7 (2014) 2577–2592.
[3] H. Scherrer, S. Scherrer, Thermoelectric properties of bismuth antimony telluride solid solutions, in: D.M. Rowe (Ed.), Thermoelectrics Handbook: Macro to Nano, CRC Taylor and Francis, Boca Raton, FL, USA, 2012.
[4] H. Kitagawa, T. Nagamori, T. Tatsuta, T. Kitamura, Y. Shinohara, Y. Noda, Liquid phase growth of $Bi_{0.5}Sb_{1.5}Te_3$ by sliding-boat method, Scr. Mater. 49 (2003) 309–313.
[5] D.B. Hyun, T.S. Oh, J.S. Hwang, J.D. Shim, N.V. Kolomoets, Electrical and thermoelectric properties of 90% Bi_2Te_3-5% Sb_2Te_3-5% Sb_2Se_3 single crystals doped with SbI_3, Scr. Mater. 40 (1998) 49–56.
[6] S. Miura, Y. Satob, K. Fukuda, K. Nishimura, K. Ikeda, Texture and thermoelectric properties of hot-extruded Bi_2Te_3 compound, Mater. Sci. Eng. A 277 (2000) 244–249.
[7] O. Ivanov, O. Maradudina, R. Lyubushkin, Preparation and characterization of bulk composite constructed of Bi_2Te_3@SiO_2 nanoparticles, J. Alloys Compd. 586 (2014) 679–682.
[8] W. Liu, X. Yan, G. Chen, Z. Ren, Recent advances in thermoelectric nanocomposities, Nano Energy 1 (2012) 42–56.
[9] Y. Li, J. Jiang, G. Xu, W. Li, L. Zhou, Y. Li, P. Cui, Synthesis of micro/nanostructured p-type $Bi_{0.4}Sb_{1.6}Te_3$ and its thermoelectrical properties, J. Alloys Compd. 480 (2009) 954–957.
[10] S.S. Kim, S. Yamamoto, T. Aizawa, Thermoelectric properties of anisotropy-controlled p-type Bi-Te-Sb system via bulk mechanical alloying and shear extrusion, J. Alloys Compd. 375 (2004) 107–113.
[11] Y. Morisaki, H. Araki, H. Kitagawa, M. Orihashi, K. Hasezaki, K. Kimura, Bi_2Te_3-related thermoelectric samples with aligned-texture prepared by plastic deformation, Mater. Trans. 46 (2005) 2518–2524.
[12] X.K. Duan, K.G. Hu, D.H. Ma, W.N. Zhang, Y.Z. Jiang, S.C. Guo, Microstructure and thermoelectric properties of $Bi_{0.5}Na_{0.02}Sb_{1.48-x}In_xTe_3$ alloys fabricated by vacuum melting and hot pressing, Rare Met. 34 (2015) 770–775.
[13] P. Srivastava, K. Singh, Effects of Cs-doping on morphological, optical and electrical properties of Bi_2Te_3 nanostructures, Mater. Lett. 136 (2014) 337–340.
[14] B. Jarivala, D. Shah, N.M. Ravindra, Transport property measurements in doped Bi_2Te_3 single crystals obtained via zone melting method, J. Electron. Mater. 44 (2015) 1509–1516.
[15] O. Ivanov, O. Maradudina, R. Lyubushkin, Grain size effect on electrical resistivity of bulk nanograined Bi_2Te_3 material, Mater. Char. 99 (2015) 175–179.
[16] Y. Pan, T.R. Wei, C.F. Wu, J.F. Li, Electrical and thermal transport properties of spark plasma sintered n-type $Bi_2Te_{3-x}Se_x$ alloys: the combined effect of point defect and Se content, J. Mater. Chem. C 3 (2015) 10583–10589.
[17] L. Hu, T. Zhu, X. Liu, X. Zhao, Point defect engineering of high-performance bismuth-telluride-based thermoelectric materials, Adv. Funct. Mater. 24 (2014) 5211–5218.
[18] J. Suh, K.M. Yu, D. Fu, X. Liu, F. Yang, J. Fan, D.J. Smith, Y.H. Zhang, J.K. Furdyna, C. Dames, W. Walukiewicz, J. Wu, Simultaneous enhancement of electrical conductivity and thermopower of Bi_2Te_3 by multifunctionality of native defects, Adv. Mater. 27 (2015) 3681–3686.
[19] J. Yang, F. Wu, Z. Zhu, L. Yao, H. Song, X. Hu, Thermoelectrical properties of lutetium-doped Bi_2Te_3 bulk samples prepared from flower-like nanopowders, J. Alloys Compd. 619 (2015) 401–405.
[20] X.H. Ji, X.B. Zhao, Y.H. Zhang, B.H. Lu, H.L. Ni, Synthesis and properties of rare earth containing Bi_2Te_3 based thermoelectric alloys, J. Alloys Compd. 387 (2005) 282–286.
[21] F. Wu, H. Song, J. Jia, X. Hu, Effects of Ce, Y, and Sm doping on the thermoelectric properties of Bi_2Te_3 alloy, Prog. Nat. Sci. Mater. Int. 23 (2013) 408–412.
[22] F. Wu, W. Shi, X. Hu, Preparation and thermoelectric properties of flower-like nanoparticles of Ce-Doped Bi_2Te_3, Electron. Mater. Lett. 11 (2015) 127–132.
[23] X.H. Ji, X.B. Zhao, Y.H. Zhang, B.H. Lu, H.L. Ni, Solvothermal synthesis and thermoelectric properties of lanthanum contained Bi–Te and Bi–Se–Te alloys, Mater. Lett. 59 (2005) 682–685.
[24] F. Wu, H.Z. Song, J.F. Jia, F. Gao, Y.J. Zhang, X. Hu, Thermoelectric properties of Ce-doped n-type $Ce_xBi_{2-x}Te_{2.7}Se_{0.3}$ nanocomposites, Phys. Status Solid A 210 (2013) 1183–1189.
[25] W.Y. Shi, F. Wu, K.L. Wang, J.J. Yang, H.Z. Song, X.J. Hu, Preparation and thermoelectric properties of yttrium-doped Bi_2Te_3 flower-like nanopowders, Electron. Mater. 43 (2014) 3162–3168.
[26] X.B. Zhao, Y.H. Zhang, X.H. Ji, Solvothermal synthesis of nano-sized $La_xBi_{(2-x)}Te_3$ thermoelectric powders, Inorg. Chem. Commun. 7 (2004) 386–388.
[27] O. Ivanov, M. Yaprintsev, R. Lyubushkin, O. Soklakova, Enhancement of thermoelectric efficiency in Bi_2Te_3 via rare earth element doping, Scr. Mater. 146 (2018) 91–94.
[28] M. Yaprintsev, R. Lyubushkin, O. Soklakova, O. Ivanov, Effects of Lu and Tm doping on thermoelectric properties of Bi_2Te_3, J. Electron. Mater. 47 (2018) 1362–1370.
[29] O. Ivanov, M. Yaprintsev, Mechanisms of thermoelectric efficiency enhancement in Lu-doped Bi_2Te_3, Mater. Res. Express 5 (2018) 015905 (1-10).
[30] (a) M. Yapryntsev, A. Vasiliev, O. Ivanov, Sintering temperature effect on thermoelectric properties and microstructure of the grained $Bi_{1.9}Gd_{0.1}Te_3$ compound, J. Eur. Ceram. Soc. 39 (4) (2019) 1193–1205;
(b) S.D. Bhame, D. Pravarthana, W. Prellier, J.G. Noudem, Enhanced thermoelectric performance in spark plasma textured bulk n-type $Bi_2Te_{2.7}Se_{0.3}$ and p-type $Bi_{0.5}Sb_{1.5}Te_3$, Appl. Phys. Lett. 102 (2013) 2190-1-3.
[31] X.A. Fan, J.Y. Yang, R.G. Chen, H.S. Yun, W. Zhu, S.Q. Bao, X.K. Duan,

Characterization and thermoelectric properties of p-type 25%Bi_2Te_3–75%Sb_2Te_3 prepared via mechanical alloying and plasma activated sintering, J. Phys. D: Appl. Phys. 39 (2006) 740–745.
[32] J. Jiang, L. Chen, S. Bai, Q. Yao, Q. Wang, Fabrication and thermoelectric performance of textured n-type $Bi_2(Te,Se)_3$ by spark plasma sintering, Mater. Sci. Eng. B 117 (2005) 334–338.
[33] Q. Lognon, F. Gascoin, O.I. Lebedev, L. Lutterotti, S. Gascoin, D. Chateigner, Quantitative texture analysis of spark plasma textured n-Bi_2Te_3, J. Am. Ceram. Soc. 97 (2014) 2038–2045.
[34] A. Vasil'ev, M. Yaprintsev, O. Ivanov, E. Danshina, Anisotropic thermoelectric properties of $Bi_{1.9}Lu_{0.1}Te_{2.7}Se_{0.3}$ textured via spark plasma sintering, Solid State Sci. 84 (2018) 28–430.
[35] M. Yapryntsev, A. Vasiliev, O. Ivanov, Sintering temperature effect on thermoelectric properties and microstructure of the grained $Bi_{1.9}Gd_{0.1}Te_3$ compound, J. Eur. Ceram. Soc. 39 (2019) 1193–1205.
[36] H. Fang, J.-H. Bahk, T. Feng, Z. Cheng, A.M. Mohammed, X. Wang, X. Ruan, A. Shakouri, Y. Wu, Thermoelectric properties of solution synthesized n-type Bi_2Te_3 nanocomposites modulated by Se: an experimental and theoretical study, Nano Res. 9 (2016) 117–127.
[37] J. Lee, A. Berger, L.U. Cagnon, U. Gosele, K. Nielsch, J. Lee, Disproportionation of thermoelectric bismuth telluride nanowires as a result of the annealing process, Phys. Chem. Chem. Phys. 12 (2010) 15247–15250.
[38] P. Lost'ák, C. Drasar, D. Bachan, L. Benes, A. Krejcová, Defects in $Bi_2Te_{3-x}Se_x$ single crystals, Radiat. Eff. Defects Solids 165 (2010) 211–215.
[39] Y.Q. Jia, Crystal radii and effective ionic radii of the rare earth ions, J. Solid State Chem. 95 (1991) 184–187.
[40] F.J. Humphreys, M. Hatherly, Recrystallization and Related Annealing Phenomena, Elsevier, Oxford, UK, 2004.
[41] J. Burke, D. Turnbull, Recrystallization and grain growth, Prog. Met. Phys. 3 (1952) 220–292.
[42] O. Ben-Yehuda, R. Shuker, Y. Gelbstein, Z. Dashevsky, M.P. Dariel, Highly textured Bi_2Te_3-based materials for thermoelectric energy conversion, J. Appl. Phys. 101 (2007) 113707-1-6.
[43] J.J. Shen, L.P. Hu, T.J. Zhu, X.B. Zhao, The texture related anisotropy of thermoelectric properties in bismuth telluride based polycrystalline alloys, Appl. Phys. Lett. 99 (2011) 124102-1-3.
[44] K.C. Lukas, W.C. Liu, Z.F. Ren, C.P. Opeil, Transport properties of Ni, Co, Fe, Mn doped $Cu_{0.01}Bi_2Te_{2.7}Se_{0.3}$ for thermoelectric device applications, J. Appl. Phys. 112 (2012) 054509-1-5.
[45] A.J. Minnich, M.S. Dresselhaus, Z.F. Ren, G. Chen, Bulk nanostructured thermoelectric materials: current research and future prospects, Energy Environ. Sci. 2 (2009) 466–479.
[46] A. Bulusu, D.G. Walker, Review of electronic transport models for thermoelectric materials, Superlattices Microstruct. 44 (2008) 1–36.
[47] A.V. Mayadas, M. Shatzkes, Electrical-resistivity model for polycrystalline films: the case of arbitrary reflection at external surfaces, Phys. Rev. B 1 (1970) 1382–1388.
[48] S. Riedel, J. Röber, T. Geßner, Electrical properties of copper films produced by MOCVD, Microelectr. Eng. 33 (1997) 165–172.
[49] J. Seo, K. Park, D. Lee, C. Lee, Microstructure and thermoelectric properties of p-type $Bi_{0.5}Sb_{0.5}Te_{0.5}$ compounds fabricated by hot pressing and hot extrusion, Scr. Mater. 38 (1998) 477–484.
[50] H.J. Goldsmid, J.W. Sharp, Estimation of the thermal band gap of a semiconductor from Seebeck measurements, J. Electron. Mater. 28 (1999) 869–872.
[51] H. Kim, Z. Gibbs, Y. Tang, H. Wang, G. Snyder, Characterization of Lorenz number with Seebeck coefficient measurement, Appl. Mater. 3 (2015) 041506-1-5.
[52] J.S. Blakemore, Solid State Physics, Cambridge University Press, Cambridge, 1985.
[53] S. Wang, J. Yang, T. Toll, J. Yang, W. Zhang, X. Tang, Conductivity-limiting bipolar thermal conductivity in semiconductors, Sci. Rep. 5 (2015) 10136-1-5.